

## Full length article

Janus Aluminum Oxysulfide  $\text{Al}_2\text{OS}$ : A promising 2D direct semiconductor photocatalyst with strong visible light harvesting

Zakaryae Haman <sup>a,\*</sup>, Nabil Khossossi <sup>a,b,\*\*</sup>, Moussa Kibbou <sup>a</sup>, Ilyas Bouziani <sup>a</sup>, Deobrat Singh <sup>a</sup>, Ismail Essaoudi <sup>a</sup>, Abdelmajid Ainane <sup>a,b,\*</sup>, Rajeev Ahuja <sup>b,c,\*</sup>

<sup>a</sup> Laboratoire de Physique des Matériaux et Modélisations des Systèmes, (LP2MS), Faculty of Sciences, Department of Physics, Moulay Ismail University, Meknes, Morocco

<sup>b</sup> Condensed Matter Theory Group, Materials Theory Division, Department of Physics and Astronomy, Uppsala University, Box 516, 75120 Uppsala, Sweden

<sup>c</sup> Department of Physics, Indian Institute of Technology Ropar, Rupnagar 140001, Punjab, India

## ARTICLE INFO

## Keywords:

2D Janus Aluminum Oxysulfide  
Optical absorption  
Photocatalytic activity  
HER  
External electric field  
Bi-axial strain  
Density functional theory

## ABSTRACT

Hydrogen production via solar light-driven water dissociation has been regarded as an artificial and effective process to overcome the environmental problem as well as solving the current energy crisis. In this regard, numerous works have mainly been devoted to developing the appropriate photocatalyst which satisfies the conditions for water splitting and understanding the photocatalysis process. In this study, we propose for the first time the potential application of the two-dimensional Janus aluminum oxysulfide  $\text{Al}_2\text{OS}$  as an efficient photocatalyst material for hydrogen-production  $\text{H}_2$  through the first-principles calculations. Janus  $\text{Al}_2\text{OS}$  monolayer has been designed from the parental binary aluminum sulfide  $\text{AlS}$  by substituting one sub-layer of sulfide atoms (S) to oxygen atoms (O). The electronic properties of the pristine  $\text{AlS}$  and the derived Janus  $\text{Al}_2\text{OS}$  were computed using GGA-PBE and HSE06 functionals. According to the band structure,  $\text{AlS}$  monolayer shows a semiconductor behavior with an indirect bandgap of 2.14 eV whereas, the Janus  $\text{Al}_2\text{OS}$  exhibits a direct bandgap of 1.579 eV. Motivated by the desirable bandgap of the Janus  $\text{Al}_2\text{OS}$ , the absorption-coefficient of Janus  $\text{Al}_2\text{OS}$  shows strong visible light harvesting compared to the parental  $\text{AlS}$ . Furthermore, the photocatalytic performance of  $\text{Al}_2\text{OS}$  has been investigated. Our calculations demonstrate that the band edge position of  $\text{Al}_2\text{OS}$  is suitable for the hydrogen evolution reaction (HER). More importantly, based on the reaction coordinate, it was found that the Gibbs free-energy  $\Delta G_{\text{H}^+}$  of  $\text{Al}_2\text{OS}$  is 0.97 eV which is smaller than of the two-dimensional Janus  $\text{Ga}_2\text{XY}$  ( $X, Y = \text{S}, \text{Se}, \text{Te}$  with  $X \neq Y$ ) reported recently. Moreover, this value decreases from 0.97 eV to 0.69 eV under 0.5 V/Å of an external electrical field. Our results indicate that Janus  $\text{Al}_2\text{OS}$  fulfills the fundamental requirements for efficient photo-catalyst under visible light and provides new guidance for hydrogen-production via water splitting.

## 1. Introduction

Regardless of the source of energy, global energy needs have skyrocketed dramatically due to the industry sectors, transportation, and population growth. Today, human activities rely mainly on non-renewable resources such as natural gas, oil, and coal known as fossil fuels [1–3]. So, the availability of these resources is declining very rapidly and their consumptions generate considerable carbon dioxide which is the main cause of greenhouse gas responsible for global warming [4]. Thus, to address these concerns, the development of a

renewable, ecological, and affordable energy source has been the subject of several researches during the last decades [5,6]. In this regard, hydrogen has been considered as an ideal energy carrier especially because it can be produced and stored from any energy source with different techniques, emits little or no pollutants during its use, and possesses high energy density [7–10]. Over the decades, photocatalysis has been recognized as an innovative and promising way to produce hydrogen from renewable energies [11,12]. Indeed, the dissociation of water (water-splitting), demonstrated by Fujishima and Honda in a photo-electro-catalytic cell has opened a promising way to produce

\* Corresponding authors.

\*\* Corresponding author at: Condensed Matter Theory Group, Materials Theory Division, Department of Physics and Astronomy, Uppsala University, Box 516, 75120 Uppsala, Sweden.

E-mail addresses: [zakaryae.haman@edu.umi.ac.ma](mailto:zakaryae.haman@edu.umi.ac.ma) (Z. Haman), [nabil.khossossi@physics.uu.se](mailto:nabil.khossossi@physics.uu.se) (N. Khossossi), [a.ainane@fs-umi.ac.ma](mailto:a.ainane@fs-umi.ac.ma) (A. Ainane), [rajeev.ahuja@physics.uu.se](mailto:rajeev.ahuja@physics.uu.se) (R. Ahuja).

hydrogen from a light source [13]. Generally, photocatalytic Water-Splitting is a technique that uses light activation (photons) for the decomposition of water. This technique has the simplicity of using a photocatalyst (semiconductor), a light source (photons), and water to produce hydrogen and oxygen cleanly without having harmful effects on the environment or producing greenhouse gases. The mechanism of dissociation of water, in an aqueous medium, follows two half-reactions electrochemical: oxidation of water by photogenerated holes and reduction of protons by electrons ( $e^-$ ) photogenerated. To bring about these reactions, the choice of the photocatalyst is crucial and should require some properties, such as a conduction band BC with an electrochemical potential lower than that of the redox couple  $H^+/H_2$  to reduce hydrogen and have a valence band BV with an electrochemical potential higher than that of the redox couple  $O_2/H_2O$  to oxidize water, but also have a bandgap allowing the absorption of wavelengths corresponding to the solar spectrum to take advantage of this important energy source [14–18]. Consequently, several efforts have been devoted to developing suitable semiconductors for photocatalysis [19–21].

Since the realization of graphene nanosheet in 2004, various families of two-dimensional compounds have been demonstrated considerable potential for exploitation in photocatalytic water splitting [16,22–25]. Among these families, Transition metal dichalcogenides (TMDs), phosphorene, g-C<sub>3</sub>N<sub>4</sub>, CdS, ZnO, SrTiO<sub>3</sub>, and WO<sub>3</sub> [26–32]. Recently, group III–VI monochalcogenides with the chemical formula MX(M = Ga, In and Al, X = S, Se, and Te) have been shown high photocatalytic performance owing to their appropriate bandgap, high surface area, suitable band alignment, and high absorption in the ultraviolet and the visible regions [17,33,34]. Furthermore, the photocatalytic efficiency can be enhanced by several methods including extrinsic/intrinsic defects, external field, heterostructures, and heterojunctions [35,36]. More recently, Janus MoSSe monolayer has been prepared experimentally by breaking the structural symmetry in MoS<sub>2</sub> nanosheet, leading to a new degree of freedom that the performance of the photocatalyst can be improved [37]. Compared to the pristine counterpart, Janus MoSSe monolayer revealed superior and distinct physical properties such as large Rashba spin splitting, strong piezoelectric effects, also it has been investigated as a promising semiconductor photocatalyst for water-splitting [38]. Importantly, derived Janus monolayers of group III monochalcogenides have been shown to fulfill the criteria of an ideal photocatalyst. For example, Huang et al. theoretically demonstrated that Janus M<sub>2</sub>XY (M = Ga and In, X/Y = S, Se, and Te) monolayers are promising photocatalysts for hydrogen evolution reaction (HER) [39,40]. Yu et al. studied the active sites of Janus Ga<sub>2</sub>XY (X/Y = O, S, Se, and Te) by evaluating Gibbs free-energy [41]. In addition, Demirtas et al. have predicted Janus aluminum monochalcogenides Al<sub>2</sub>XY(X/Y = O, S, Se, and Te) starting from the binary AlX (X = O, S, Se, Te) compounds [42].

Intriguingly, the intrinsic dipole moment, which is created by the structural asymmetry along the z-direction in Janus Al<sub>2</sub>OS offers an extra degree of freedom in order to ameliorate the spacial separation between the photo-induced charge (electrons and holes) into different surfaces and subsequent could enhance the photocatalytic conversion efficiency. Motivated by this strategy to improve the HER and the unique properties of the Janus structures, we have investigated the photocatalytic activity of Janus Al<sub>2</sub>XY monolayer and rigorously compared with the parental AIS by means of the density functional theory. Our present study not only demonstrates the superior properties of Janus Al<sub>2</sub>OS monolayer but also highlights the efficiency of Janus structure to prevent the carrier recombination and improve the hydrogen evolution reaction.

## 2. Computational frameworks

In this study, electronic, optical as well as photocatalytic performance of the pristine AIS and the derived Janus Al<sub>2</sub>OS were investigated on the basis of Density Functional Theory (DFT) implemented

in the Vienna Ab Initio Simulation Package (VASP) [43] code. The Projector Augmented Wave (PAW) was used to describe electron-ion interactions. The exchange correlation functional was computed using the generalized gradient approximation (GGA) in the form of Perdew–Burke–Ernzerhof (PBE) functional with a kinetic-energy cutoff of about 600 eV. Geometry optimizations were performed by setting the convergence criteria for energy and force at  $10^{-6}$  eV and  $10^{-4}$  eV/Å, respectively. In addition, to obtain an accurate bandgap value of our materials and understand the electronic trend, we used the Heyd Scuseria Ernzerhof (HSE) exchange correlation functional with parameters of ( $\alpha = 0.25$  and  $\mu = 0.20$ ) which provides an optimal band gap for a variety of semiconductors [44,45]. To avoid the interaction between stacked layers and periodic pictures, the vacuum layer was set to 20 Å in the c-direction during geometry optimization. A Monkhorst Pack K-Point grid of  $11 \times 11 \times 1$ ,  $24 \times 24 \times 1$ , and  $32 \times 32 \times 1$  is used in the reciprocal space during geometrical optimization, electronic density of states, and optical properties, respectively [46]. The Grimme dispersion correction DFT-D3 approach [47] was implemented in order to involve the wide range van-der-Waals (vdW) interaction for the Hydrogen adsorption on the Janus Al<sub>2</sub>OS lattice. The dipole correction is employed during our calculation in order to remove the artificial electric-field in the vacuum-region [48]. The lattice dynamical stability was checked by the phonon dispersion calculation using Phonopy code with density functional perturbation (DFPT) method [49–51] with  $(5 \times 5 \times 1)$ -super-cell in order to ensure the convergence and yield accurate output. Additionally, the thermal stability was checked with ab-initio molecular dynamics (AIMD) simulations [52,53] at 600 K for 9ps using DFT/GGA theory and the PBE exchange correlation functional within canonical ensemble (NVT). Our recent publications provide more information about the computational methods [25,54].

## 3. Results and discussion

### 3.1. Structural and electronic properties

The atomic structure of the optimized two-dimensional aluminum sulfide AIS is depicted in Fig. 1(a) AIS monolayer is one of the binary group III–V compounds, which has a honeycomb crystalline structure with  $D_{3h}$  point-symmetry group similar to the GaS and GaSe nanosheets [55]. The primitive cell of aluminum sulfide AIS is made by four atomic sublayers stacking as Al–S–S–Al. The structural parameters reveal that at the equilibrium, the Bravais vectors of AIS monolayer is  $a = b = 3.579$  Å, and Al–S interatomic distance is  $d_{Al-S} = 2.325$  Å. (see Table 1). Our findings are very close to the previous theoretical reports [34,56]. Based on the structure of AIS monolayer, Demirtas et al. have designed a new structure known as Janus Al<sub>2</sub>OS by substituting one sub-layer of sulfide atoms (S) to oxygen atoms (O) [42]. The top and side views of the derived Janus Al<sub>2</sub>OS are presented in Fig. 1(a) and (b). It is worth mentioning that the Janus Al<sub>2</sub>OS shares a hexagonal crystalline structure similar to the pristine AIS in which the double layer of aluminum Al–Al is sandwiched between the sulfide and the oxygen layers leading to a sequence of S–Al–Al–O. The computed structural parameters of the Al<sub>2</sub>OS monolayer are summarized in Table 1. One can notice that the lattice parameter of the Janus Al<sub>2</sub>OS ( $a = b = 3.776$  Å) is larger than of the parental AIS ( $a = b = 3.579$  Å). The thermal and dynamic stability of the considered structure were confirmed by ab-initio molecular dynamics (AIMD) simulation at 600 K with a time scale of 9 fs and phonon dispersion, respectively. By the appearance of all positive frequency modes with a complete absence of negative values over the full symmetry of the Brillouin zone, the Al<sub>2</sub>OS monolayer demonstrates excellent dynamic stability as shown in Fig. 2(a). Furthermore, Fig. 2(b) shows the variation of the total energy as a function of dynamic steps in the simulations for the Janus monolayer, with the corresponding screenshot taken at the end of the dynamic simulations. One can notice that there is no significant deformation after the dynamic simulations indicating that our compound

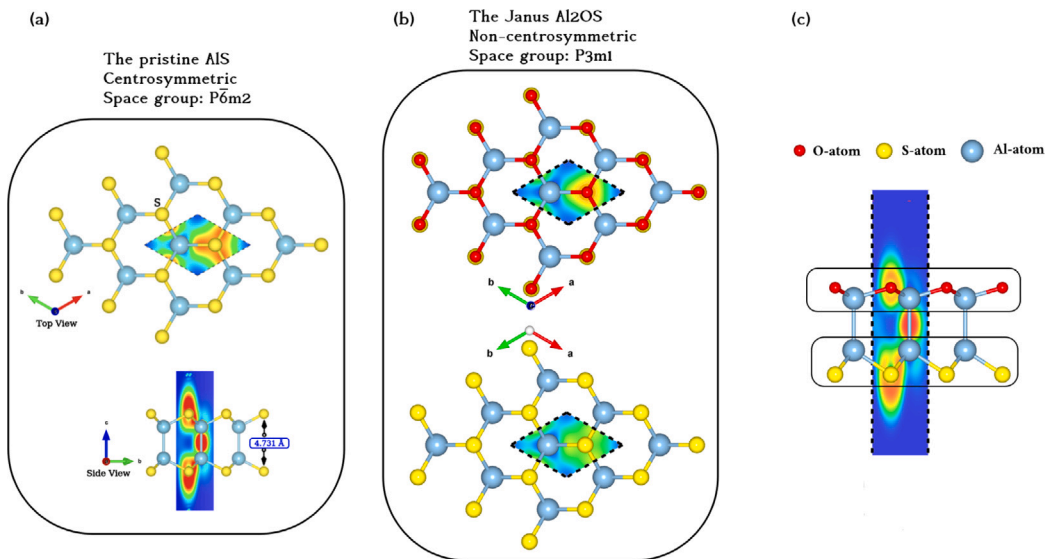


**Fig. 1.** (a)–(b) Top and side view of the parental AIS and Janus Al<sub>2</sub>OS monolayers respectively. (c) Side snapshot of electron charge density of Janus Al<sub>2</sub>OS nanosheet. The dashed lines refers to the hexagonal unit cell.

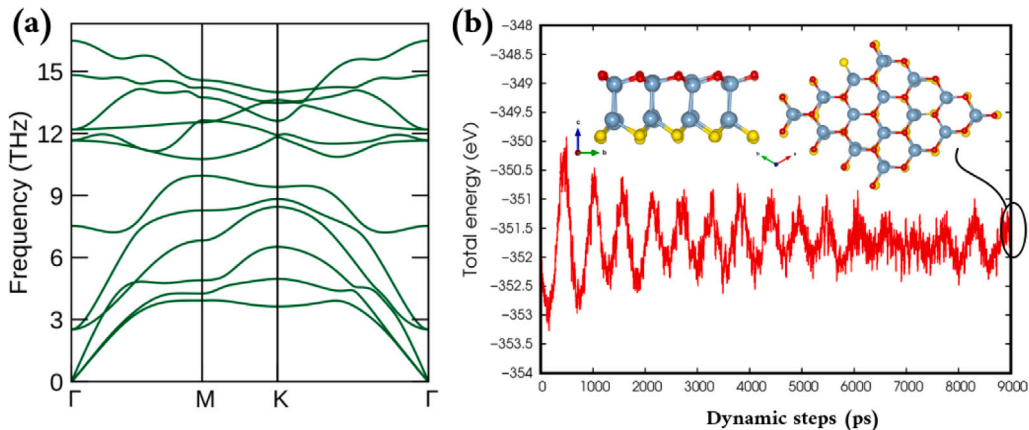


**Fig. 2.** (a) Phonon dispersion spectra and (b) the change in total energy with average force at 600 K as a function of time for Al<sub>2</sub>OS monolayer.

keeps the initial structure without any bond distortion. Meanwhile, the total energy variation remains almost unchanged throughout the dynamic simulations. This confirms the exceptional dynamic stability of the Al<sub>2</sub>OS monolayer. In addition, due to the difference of electronegativity and the atomic radius between the sulfide and oxygen atoms, the structural symmetry of the parental AIS is broken resulting to inequivalent Al-O and Al-S bond lengths (see Table 1). Moreover, an intrinsic dipole moment in the out-of-plane direction is constructed with a value of 0.432 D (see Table 1), which gives rise to an internal electric field. Subsequently, from Fig. 3(a) no electrostatic potential difference is observed in the pristine AIS monolayer between two sulfide atoms. Contrary to AIS, a potential energy difference is observed in the Janus Al<sub>2</sub>OS between the vacuum levels at the two respective surfaces as illustrated in Fig. 3(b) and Table 1.

On the basis of the optimized AIS and Al<sub>2</sub>OS structures, the computed electronic band structures of the pristine AIS and the derived Janus Al<sub>2</sub>OS along the highly symmetric  $\Gamma$ –M–K– $\Gamma$  path in the first Brillouin zone are presented in Figs. 4 and 5 using GGA–PBE and HSE06 functionals. Fig. 4 reveals that the aluminum sulfide is an indirect semiconductor with a bandgap of 2.10 eV/2.88 eV using GGA–PBE/HSE06 functionals. These results are very close to the previous theoretical reports [34]. The Janus Al<sub>2</sub>OS preserves the semiconductor characteristic with a direct bandgap of 1.579 eV/2.111 eV using GGA–PBE/HSE06 (see Fig. 5 and Table 1). More precisely,

**Table 1**

Selected geometrical and electronic parameters of the parental AIS and the derived Janus Al<sub>2</sub>OS monolayers: lattice parameters  $a$  (Å), bond lengths  $d_{Al-X}$  (Å), thickness  $h$  (Å), electronic band gaps using PBE and HSE06 exchange-correlation functionals, and Work Function (WF).

| Materials          | $a = b$<br>(Å) | $d_{Al-Al}$<br>(Å) | $d_{Al-(O/S)}$<br>(Å) | $h$<br>(Å) | $E_g^{PBE}$<br>(eV) | $E_g^{HSE06}$<br>(eV) |
|--------------------|----------------|--------------------|-----------------------|------------|---------------------|-----------------------|
| AIS                | 3.579          | 2.598              | 2.325                 | 4.731      | 2.106               | 2.887                 |
| Al <sub>2</sub> OS | 3.776          | 2.586              | 1.951/2.237           | 4.378      | 1.579               | 2.111                 |

the Valence band maximum of the parental AIS is located at the valley  $K - \Gamma$ , whereas the conduction band minimum is located at  $M$  point. For completeness, the total density of states and the partial density of states for AIS and Al<sub>2</sub>OS are calculated to further clarify the electronic properties of our compounds as well as elucidating the contribution of each orbital. As we can see from both Figs. 4 and 5, the conduction band minimum is mainly formed by S (2p) and O (2p), S (2p) orbitals for AIS and Al<sub>2</sub>OS respectively whereas, the valence band maximum are consisted of hybridization between Al (2p), S (2p), and O (2p) orbitals for both monolayers.

It is widely known that two-dimensional nanosheets including Janus monolayers are sensitive to strain engineering and can tune their electronic properties. In this context, we have investigated the effect of

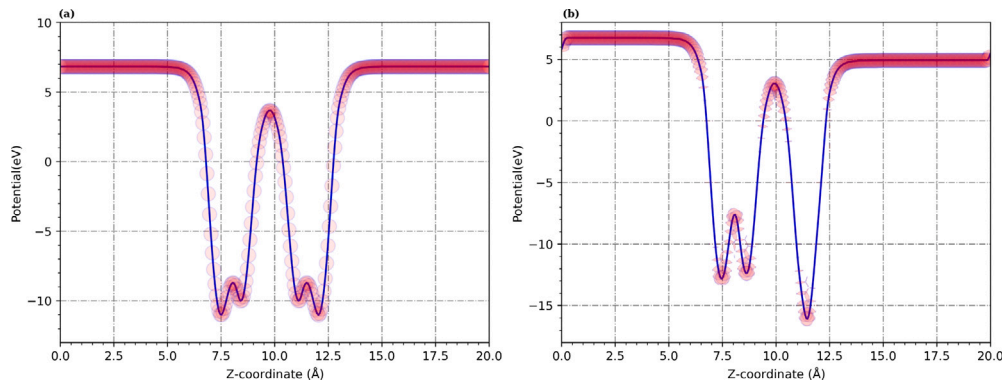


**Fig. 3.** (a,b) The planar average electrostatic potential for the pristine AIS and the Janus Al<sub>2</sub>OS respectively.

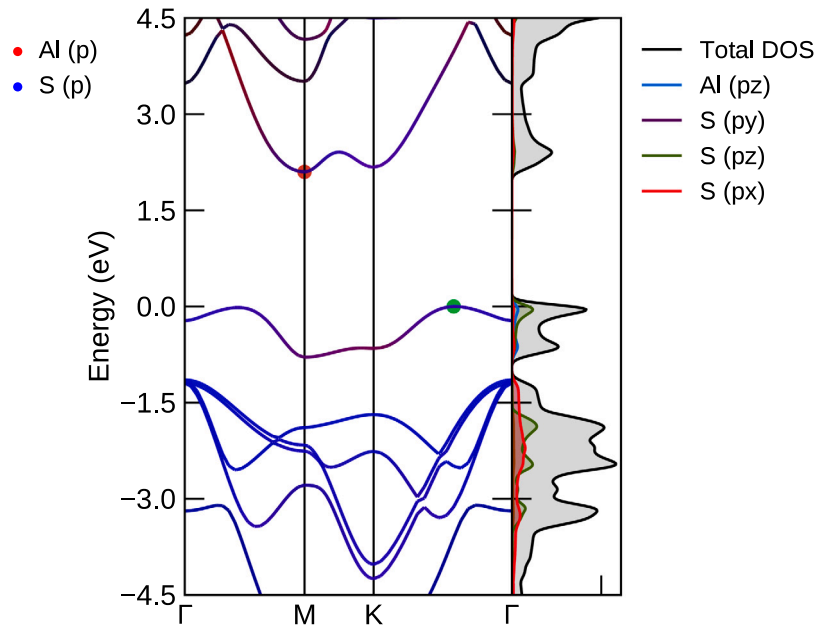


**Fig. 4.** The calculated band structure with corresponding density of state for the pristine AIS using PBE functional.

a biaxial strain  $\epsilon_b$  on the electronic properties of the two-dimensional Janus Aluminum Oxysulfide Al<sub>2</sub>OS. It is worth to mention that a biaxial strain is defined as  $\epsilon_b = \frac{a_0-a}{a_0}$ . Here,  $a_0$  and  $a$  refer respectively to the lattice parameter of Janus Al<sub>2</sub>OS before and after strain. In this study, we have applied a biaxial strain from 0 to  $\pm 10\%$  where the plus and the minus signs indicate the tensile and the compressive strain respectively.

The computed band structure of the Janus Al<sub>2</sub>OS under different values of bi-axial strain  $\epsilon_b$  is shown in Fig. 6. Our detailed findings reveal that the band structure of Janus Al<sub>2</sub>OS is remarkably influenced by biaxial strain. Thereby, the electronic properties are significantly tuned, especially in the compressive strain ( $\epsilon_b < 0$ ). From Fig. 6a, a transition from direct to indirect band gap is observed up to  $\pm 2\%$  of the tensile strain. In addition, the valence band minimum is located at the valley  $K - \Gamma$ , whereas the conduction band maximum is located at  $\Gamma$  point for different levels of tensile strain. However, in the case of compressive strain as illustrated in Fig. 6b, a transition from semiconductor to metal is found up to  $-6\%$  and a direct to indirect band gap is observed at  $-2\%$  and  $-4\%$ . For completeness, the variation of the band gap under different values of the biaxial strain are calculated using PBE and HSE06 functionals as depicted in Fig. 7.

### 3.2. Optical properties of the pristine AIS and the derived Janus Al<sub>2</sub>OS

One of the crucial steps of water-splitting is the optical response of materials to light. In this section, we present the optical properties of the pristine AIS as well as the derived Janus Al<sub>2</sub>OS monolayer. Interestingly, the optical parameters such as the absorption-coefficient, the extinction coefficient, reflectivity, and the energy loss function are determined from the frequency-dependent complex dielectric function [57, 58].

$$\epsilon(\omega) = \epsilon_1(\omega) + i\epsilon_2(\omega) \quad (1)$$

Particularly, the imaginary part of the dielectric tensor indicates all the transitions from the valence band (occupied states) to the conduction band (unoccupied states) whereas the real part is computed by the help of Kramers–Kronig transformations.

Obviously, the expression of the real and the imaginary parts of the dielectric tensor are detailed in our last works [59–61].

Based on the structural anisotropy, the real and the imaginary parts of the complex dielectric function are split in xx and zz directions as depicted in Fig. 8 using HSE06 functional. The static dielectric constants in the xx direction are found to be 3.5 and 3 for Janus Al<sub>2</sub>OS and AIS respectively. Moreover, the first peak in the imaginary part is occurred at 3 eV and 3.8 eV respectively for Janus Al<sub>2</sub>OS

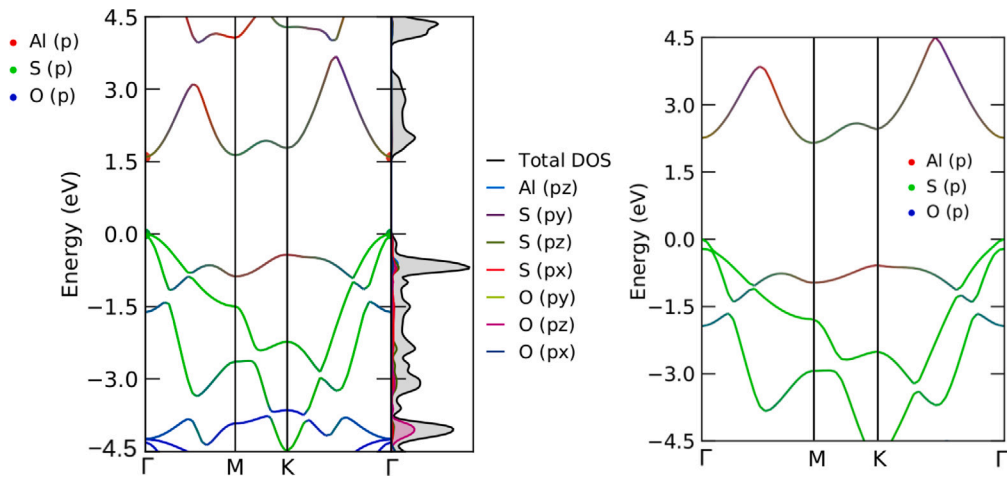


**Fig. 5.** Total and projected electronic band structure using PBE and HSE06 functionals with corresponding total and partial density of states of Janus Al<sub>2</sub>OS monolayer. The Fermi-level is set at zero.

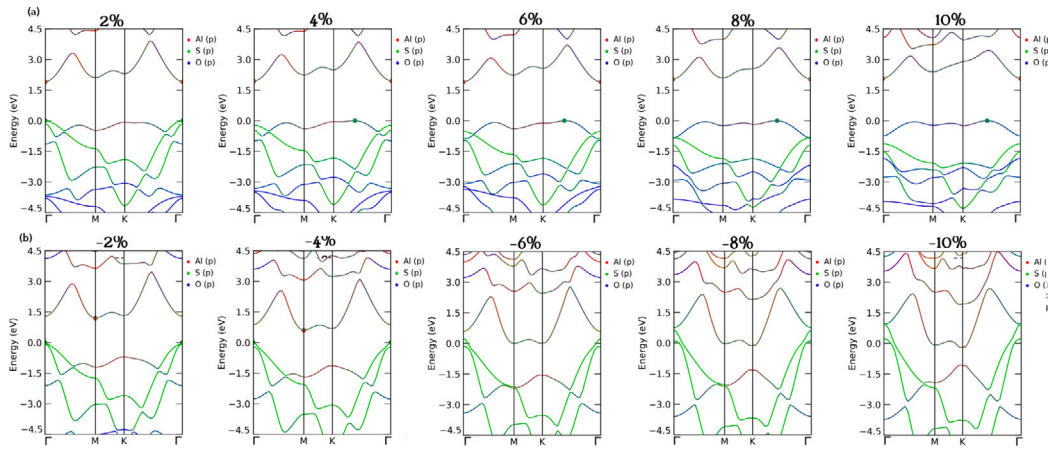


**Fig. 6.** The computed band structures of Janus Al<sub>2</sub>OS under (a) tensile (b) compressive strains using PBE functional.

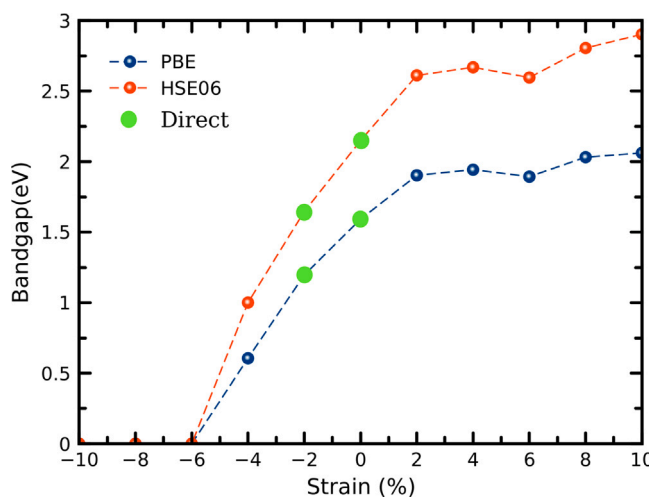


**Fig. 7.** The variation of bandgap under different levels of biaxial strain ranging from 0 to  $\pm 10\%$  using PBE and HSE06 functionals.

and AIS. In order to assess the light harvesting capability of AIS and Al<sub>2</sub>OS monolayers, the absorption-coefficient is calculated using HSE06

functional as:

$$\alpha(\omega) = \sqrt{2}\omega \left[ \sqrt{\epsilon_1(\omega)^2 + \epsilon_2(\omega)^2} + \epsilon_2(\omega) \right]^{1/2} \quad (2)$$

**Fig. 9** shows the absorption-coefficient of AIS and Al<sub>2</sub>OS in the xx and zz directions. It is clearly seen that the absorption spectrum exhibits strong anisotropy due to the structural symmetry of our materials. Moreover, the absorption-coefficient of AIS and Al<sub>2</sub>OS has followed similar behavior and can reach  $2.5 \times 10^5$  and  $3.1 \times 10^5$  at 3 eV and 3.8 eV respectively indicating that Janus Al<sub>2</sub>OS can capture light in the visible range due to low bandgaps compared to the parental AIS. Our findings demonstrate that Janus Al<sub>2</sub>OS exhibits strong absorption-coefficient compared to the most known absorber materials such as CdS and halide perovskites indicating that Janus Al<sub>2</sub>OS fulfills the condition as a good absorber and an efficient semiconductor for hydrogen-production by water-splitting [62,63].

### 3.3. Photocatalytic activity of Al<sub>2</sub>OS monolayer

In this section, we aim to provide the photocatalytic efficiency of the 2D Janus Al<sub>2</sub>OS monolayer. It is worth to mention that no electrostatic potential difference is observed in the pristine AIS due to the same atoms in the top and the bottom layers of the monolayer. On the contrary, the Janus Al<sub>2</sub>OS with the intrinsic dipole moment possesses an electro-static potential difference which generates an electrical field inside the structure along the out-plane direction. The

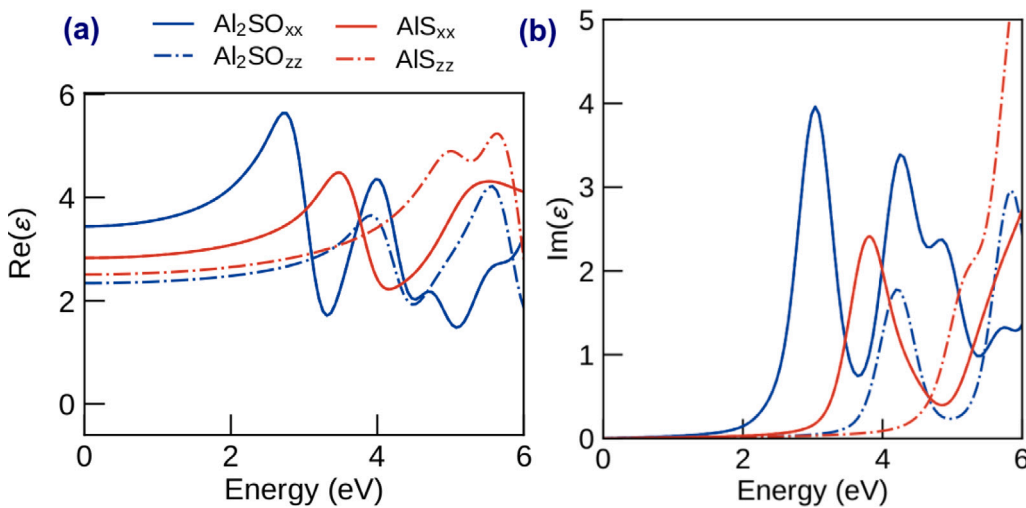


Fig. 8. (a)–(b) The real and the imaginary parts of the dielectric tensor of Janus  $\text{Al}_2\text{OS}$  using  $HSE06$  functional respectively.

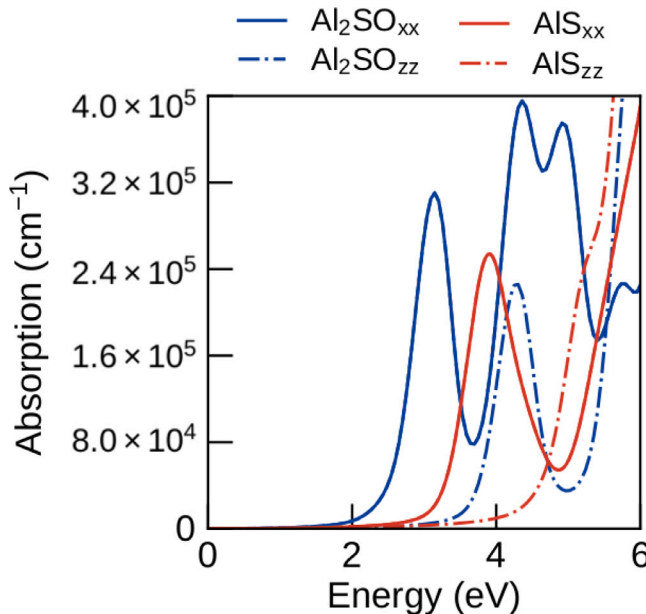


Fig. 9. The computed absorption coefficient of Janus  $\text{Al}_2\text{OS}$  monolayer using  $HSE06$  functional.

computed electro-static potential difference  $\Delta V$  between the  $S$  and  $O$  layers is 1.83 eV. Notably, the electrostatic potential difference in the Janus  $\text{Al}_2\text{OS}$  not only acts as an additional booster for the separation of the photogenerated carriers, but also violates the band gap criteria for traditional photocatalysts [27].

More importantly, the efficiency of both electron- and hole-transfer along a selected orientation is very crucial in order to get an effective charge-separation and thereby decrease the recombination efficiency, leading to an enhancement of the water-splitting activity performance. Although, the carrier mobility is commonly recognized to be inversely correlated with the effective mass, and thus a smaller effective mass of charge carriers leads to a larger carrier mobility. Consequently, for this purpose we focus in this part on the effective masses of electron and hole. The computed effective masses of both electrons and holes for the Janus  $\text{Al}_2\text{OS}$  monolayer are listed in Table 2, in which the effective mass of electrons (0.569 along  $\Gamma - M$  and 0.578 along  $\Gamma - K$ ) and holes ( $-0.962$  along  $\Gamma - M$  and  $-0.907$  along  $\Gamma - K$ ). The obtained effective mass of the electrons is relatively small as compared to the holes.

Table 2

The electrostatic potential difference  $\Delta V$ , the intrinsic dipole moment  $\mu$ , Work Function (WF), and the effective Mass of Electron and Hole for the Janus  $\text{Al}_2\text{OS}$ .

| Materials          | $\Delta V$<br>(eV) | $\mu$<br>(Debye) | WF<br>(eV) | $m_e^*/m_e$<br>$\Gamma - M$ ( $\Gamma - K$ ) | $m_h^*/m_h$<br>$\Gamma - M$ ( $\Gamma - K$ ) |
|--------------------|--------------------|------------------|------------|--|--|
| AlS                | 0                  | 0                | 6.749      | –  | –  |
| Al <sub>2</sub> OS | 1.83               | 0.432            | 6.752      | 0.569 (0.578)                                | $-0.962$ ( $-0.907$ )                        |

Therefore, the large effective mass difference between the electrons and the holes is advantageous to restrain their recombination rate [64].

For completeness a promising photocatalyst for hydrogen evolution reaction should have the suitable energy alignment of VBM and CBM. In this direction, the valence band minimum energy should be lower than the reduction potential of  $\text{H}^+/\text{H}_2$  ( $E_{\text{H}^+/\text{H}_2} = 0$  eV at pH = 0), whereas the conduction band maximum should be higher than the oxidation potential of  $\text{O}_2/\text{H}_2\text{O}$  ( $E_{\text{O}_2/\text{H}_2\text{O}} = 1.23$  eV at pH = 0). In our previous theoretical work, we have shown that the pristine AlS monolayer is a candidate photocatalyst with appropriate band edge positions. However, based on the Yang's theory and taking into consideration the electrostatic potential difference  $\Delta V$ , the reduction potential  $\text{H}^+/\text{H}_2$  will define as follows [65]:

$$E_{\text{H}^+/\text{H}_2-\text{top}} = E_{\text{H}^+/\text{H}_2} + \Delta V \quad (3)$$

In this regard the CBM is calculated based on the Mulliken electronegativity as follows:

$$E_{\text{CBM}} = \chi - E_e - E_g^{\text{HSE-06}}/2 \quad (4)$$

Where  $\chi$ ,  $E_e$  and  $E_g^{\text{HSE-06}}$  indicate the electronegativity of Janus  $\text{Al}_2\text{OS}$ , the total energy of a free-electrons which is about 4.5 eV and the band gap of our monolayer using  $HSE06$  functional respectively.

Moreover, the conduction and valence bands, respectively, generate electrons and holes when solar light is irradiated. Following that, guided by the intrinsic electric field, these photogenerated electrons transfer to the top surface, contributing to the hydrogen evolution reaction. The redox potentials of  $\text{H}^+/\text{H}_2$  and  $\text{H}_2\text{O}/\text{O}_2$  are also altered, expanding the photogenerated carriers' over-potentials ( $\Delta E_1$  and  $\Delta E_2$ ), due to the differing vacuum levels on the two sides of the Janus  $\text{Al}_2\text{OS}$  as shown in Fig. 10. More intriguingly, the  $\Delta V$  of the Janus  $\text{Al}_2\text{OS}$  monolayer is greater than 1.23 eV ( $V = 1.83$  eV), above the traditional band gap limit for total water splitting.

In addition to the band alignments energy, the hydrogen adsorption energy of the reaction intermediate  $E_{\text{H}^*}$  is computed for different adsorption sites, such as on the bridge, hollow and on the top to further

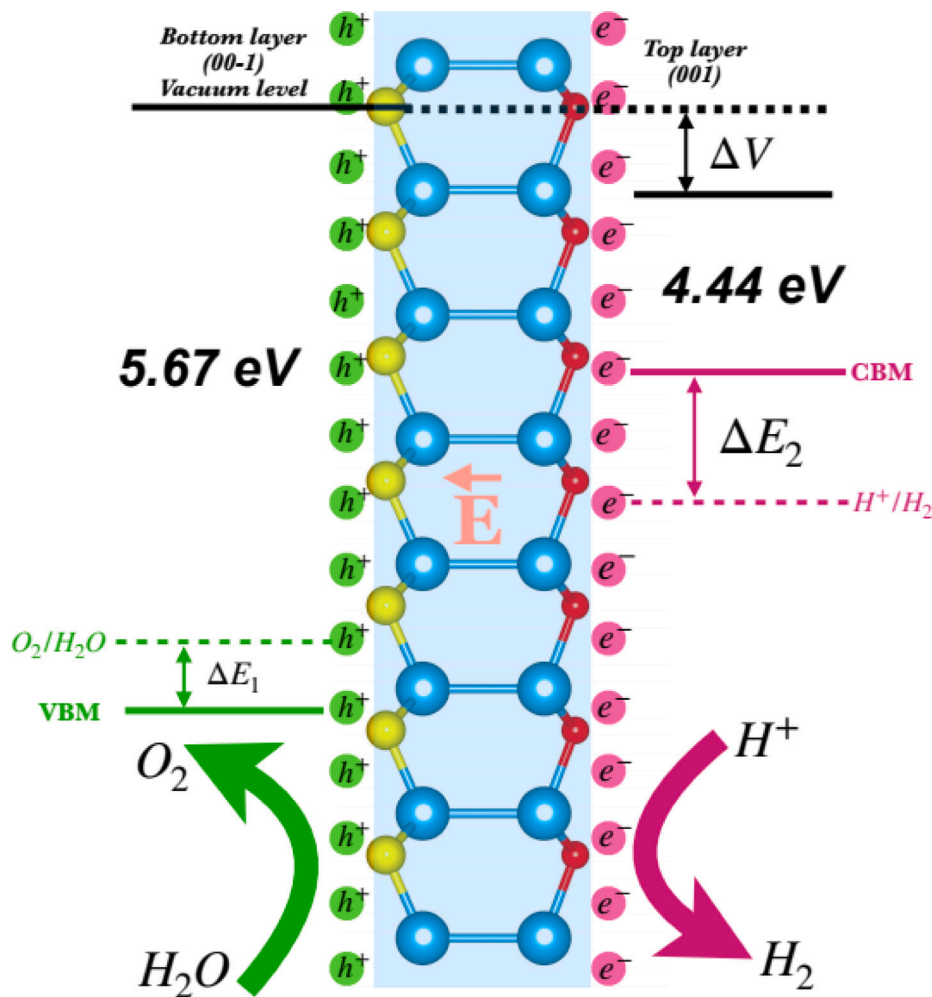


**Fig. 10.** A schematic representation of the Janus Aluminum Oxsulfide Al<sub>2</sub>OS monolayer energy levels and photocatalytic process.

explore the photocatalytic-activity of the Janus Al<sub>2</sub>OS. The hydrogen adsorption energy is obtained as follows:

$$\Delta E_{H^*} = E_{Al_2OS+H} - E_{Al_2OS} - \frac{1}{2} E_{H_2} \quad (5)$$

Where  $E_{Al_2OS+H}$  and  $E_{Al_2OS}$  are respectively termed to the total energy of the Janus Al<sub>2</sub>OS with and without H atom, whereas  $H_2$  refers to the energy of single  $H_2$ -molecule in the gas phase. Based on the hydrogen adsorption energy  $\Delta E_{H^*}$ , Gibbs free-energy  $\Delta G_{H^*}$  is a determinant descriptor for the hydrogen evolution reaction. Subsequently, according to the Sabatier rule, a good photocatalyst for water-splitting should verify the thermoneutrality criterion (i.e.  $\Delta G_{H^*}$  close to zero). The Gibbs free-energy of 2D Janus Al<sub>2</sub>OS is given by [54]:

$$\Delta G_{H^*} = \Delta E_{H^*} - T \Delta S_H + \Delta E_{ZPE} \quad (6)$$

Where  $\Delta E_{ZPE}$  and  $\Delta S_H$  are respectively the zero-point energy variation and the entropy change between the adsorbed dihydrogen ( $H_2$ ) molecule site and the gas phase. Thus, the contribution of  $\Delta E_{ZPE} - T \Delta S_H$  is 0.24 eV for the hydrogen adsorption on the Janus Al<sub>2</sub>OS monolayer. Therefore, the equation could be re-defined as follows:

$$\Delta G_{H^*} = \Delta E_{H^*} + 0.24 \quad (7)$$

The obtained Gibbs free-energy for the Janus Al<sub>2</sub>OS is listed in Table 3. It is obvious that the derived Janus has the smallest value of  $\Delta G_{H^*}$  (0.97 eV) compared to the parental AlS monolayer (1.24 eV) and to the gallium based Janus chalcogenides Ga<sub>2</sub>XY. However, this measure of  $\Delta G_{H^*}$  for Janus Al<sub>2</sub>OS is still large to the optimal (0 eV) (see Fig. 11). In order to decrease the value of  $\Delta G_{H^*}$ , we have

**Table 3**  
A comparative summary of Gibbs free energy profile  $\Delta G_{H^*}$  [34].

| 2D materials          | AlS  | Al <sub>2</sub> OS | Al <sub>2</sub> OS (with $E_z = 0.5V/A$ ) |
|-----------------------|------|--------------------|---|
| $\Delta G_{H^*}$ (eV) | 1.24 | 0.97               | 0.69                                      |

systematically applied an external electrical field along the z-direction. From Fig. 12,  $\Delta G_{H^*}$  for Al<sub>2</sub>OS decreases from 0.97 eV to 0.69 eV under 0.5 V/A of the electrical field. Furthermore, this value is still a giant gap with the optimal 0 eV and offers a new challenge to tune it using several methods such as strains and defects. Intriguingly, Janus structures are commonly possessed ferroelectric properties. However, an in-depth investigation on the paraelectric phase could offer new guidance to improve the photocatalytic performance as demonstrated recently by Lin's group [66].

#### 4. Conclusion

In summary, we have carefully presented an in-depth study to examine the photocatalytic performance for the two-dimensional Janus aluminum Oxsulfide Al<sub>2</sub>OS along with the parental Aluminum Sulfide AlS monolayer based on the binding energy and Gibbs free-energy through DFT computations. The band structure analysis indicates that the Janus Al<sub>2</sub>OS is a direct semiconductor with an appropriate bandgap of 2.11 eV using HSE06 functional. Motivated by the suitable bandgap, the absorption-coefficient and the band edge alignments of Janus Al<sub>2</sub>OS

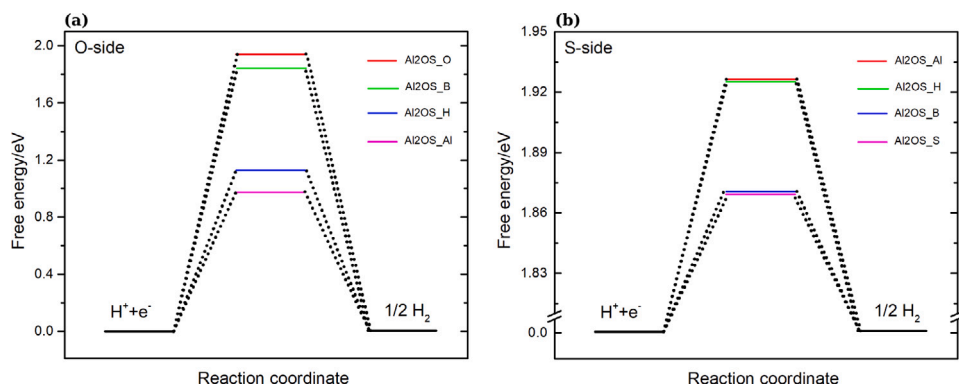


**Fig. 11.** Gibbs free energy profile: (a)–(b) The calculated Gibbs free energy of Janus Al<sub>2</sub>OS in the S and O sides respectively. (b)- The variation of Gibbs free energy under different levels of electrical field ranging from 0.1 V/A to 0.5 V/A..

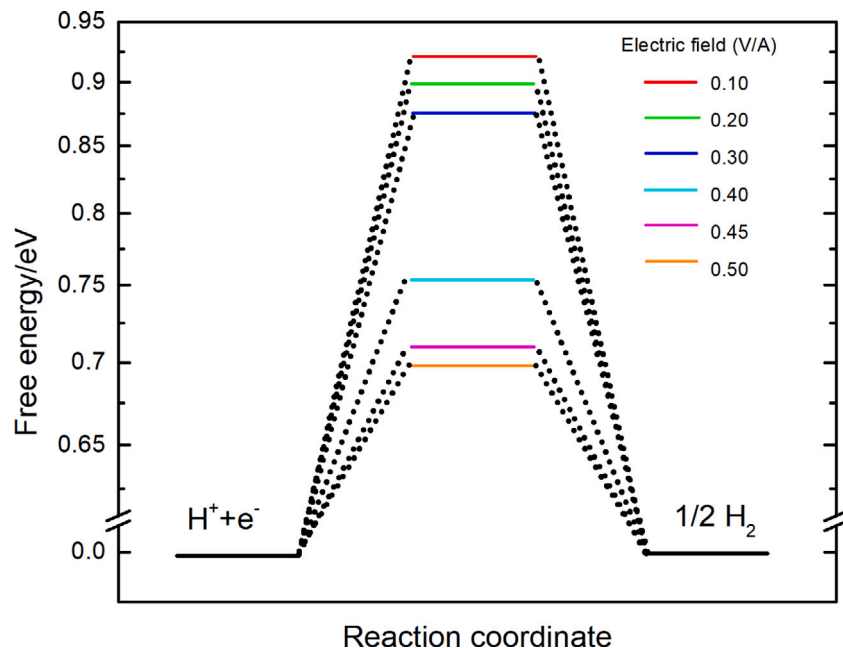


**Fig. 12.** The variation of Gibbs free energy under different levels of electrical field ranging from 0.1 V/A to 0.5 V/A.

are depicted. It is found that our material shows a strong absorption-coefficient in the visible region indicating its ability to harvest sunlight. In addition, the calculated band alignments energy of Janus Al<sub>2</sub>OS straddle the oxidation and the reduction potentials of the water. By virtue of the reaction coordinate, the Gibbs free-energy of Janus Al<sub>2</sub>OS is found to be 0.97 eV which is smaller than of the pristine AIS (1.24 eV) monolayer. To enhance the value of the hydrogen absorption energy, an external electrical field is applied along the z-direction  $E_z$ . Sub-consequently, the Gibbs free-energy decreases from 0.97 eV to 0.67 eV under 0.5 V/A of the electrical field. Our results demonstrate that the Janus Al<sub>2</sub>OS satisfies the fundamental conditions as a promising semiconductor photocatalyst for hydrogen-production via water splitting.

#### CRediT authorship contribution statement

**Zakaryae Haman:** Conceptualization, Formal analysis, Validation, Visualization, Writing – review & editing. **Nabil Khossossi:** Conceptualization, Data curation, Methodology, Formal analysis, Validation, Visualization, Writing – review & editing. **Moussa Kibou:** Formal analysis, Validation, Visualization, Writing – review & editing. **Ilyas Bouziani:** Writing – review & editing. **Deobrat Singh:** Formal analysis,

Methodology, Writing – review & editing. **Ismail Essaoudi:** Writing – review & editing. **Abdelmajid Ainane:** Supervision, Funding acquisition, Writing – review & editing. **Rajeev Ahuja:** Supervision, Funding acquisition, Software, Project administration, Writing – review & editing.

#### Declaration of competing interest

The authors declare that they have no known competing financial interests or personal relationships that could have appeared to influence the work reported in this paper.

#### Acknowledgments

N.K., D.S. & R.A. thanks the Swedish Research Council (VR-2016-06014 & VR2020-04410) and J. Gust. Richert stiftelse, Sweden (2021-00665) for financial support and the computational resources from the Swedish National Infrastructure for Computing SNIC (2020/1-40 & 2021/1-42) and HPC2N. A.A and I.E acknowledge support from the PPR2 Project, Morocco (MESRSF-CNRST).

## References

- [1] M.I. Hoffert, K. Caldeira, A.K. Jain, E.F. Haites, L.D. Harvey, S.D. Potter, M.E. Schlesinger, S.H. Schneider, R.G. Watts, T.M. Wigley, et al., Energy implications of future stabilization of atmospheric CO<sub>2</sub> content, *Nature* 395 (6705) (1998) 881–884.
- [2] I. Roger, M.A. Shipman, M.D. Symes, Earth-abundant catalysts for electrochemical and photoelectrochemical water splitting, *Nat. Rev. Chem.* 1 (1) (2017) 1–13.
- [3] M. Dresselhaus, I. Thomas, Alternative energy technologies, *Nature* 414 (6861) (2001) 332–337.
- [4] T. Hisatomi, K. Domen, Introductory lecture: sunlight-driven water splitting and carbon dioxide reduction by heterogeneous semiconductor systems as key processes in artificial photosynthesis, *Faraday Discuss.* 198 (2017) 11–35.
- [5] J.A. Turner, Sustainable hydrogen production, *Science* 305 (5686) (2004) 972–974.
- [6] M.-I. Jamesh, Y. Kuang, X. Sun, Constructing earth-abundant 3D nanoarrays for efficient overall water splitting—a review, *ChemCatChem* 11 (6) (2019) 1550–1575.
- [7] G. Marbán, T. Valdés-Solís, Towards the hydrogen economy? *Int. J. Hydrogen Energy* 32 (12) (2007) 1625–1637.
- [8] G.L. Cardoso, P.C. Piquini, N. Khossossi, R. Ahuja, Lithium-functionalized boron phosphide nanotubes (BPNTs) as an efficient hydrogen storage carrier, *Int. J. Hydrogen Energy* 46 (39) (2021) 20586–20593.
- [9] A. Olabi, A.A. Abdelghafar, A. Baroutaji, E.T. Sayed, A.H. Alami, H. Rezk, M.A. Abdelkareem, et al., Large-vscales hydrogen production and storage technologies: Current status and future directions, *Int. J. Hydrogen Energy* 46 (45) (2021) 23498–23528.
- [10] N. Khossossi, Y. Benhouria, S.R. Naqvi, P.K. Panda, I. Essaoudi, A. Ainane, R. Ahuja, Hydrogen storage characteristics of Li and Na decorated 2D boron phosphide, *Sustain. Energy Fuels* 4 (9) (2020) 4538–4546.
- [11] I. Dincer, C. Acar, Review and evaluation of hydrogen production methods for better sustainability, *Int. J. Hydrogen Energy* 40 (34) (2015) 11094–11111.
- [12] Y. Miseki, K. Sayama, Photocatalytic water splitting for solar hydrogen production using the carbonate effect and the Z-scheme reaction, *Adv. Energy Mater.* 9 (23) (2019) 1801294.
- [13] A. Fujishima, K. Honda, Electrochemical photolysis of water at a semiconductor electrode, *Nature* 238 (5358) (1972) 37–38.
- [14] M.G. Kibria, H.P. Nguyen, K. Cui, S. Zhao, D. Liu, H. Guo, M.L. Trudeau, S. Paradis, A.-R. Hakima, Z. Mi, One-step overall water splitting under visible light using multiband InGaN/GaN nanowire heterostructures, *ACS Nano* 7 (9) (2013) 7886–7893.
- [15] Q. Xiang, J. Yu, M. Jaroniec, Synergistic effect of MoS<sub>2</sub> and graphene as cocatalysts for enhanced photocatalytic H<sub>2</sub> production activity of TiO<sub>2</sub> nanoparticles, *J. Am. Chem. Soc.* 134 (15) (2012) 6575–6578.
- [16] A.K. Singh, K. Mathew, H.L. Zhuang, R.G. Hennig, Computational screening of 2D materials for photocatalysis, *J. Phys. Chem. Lett.* 6 (6) (2015) 1087–1098.
- [17] X. Zhang, Z. Zhang, D. Wu, X. Zhang, X. Zhao, Z. Zhou, Computational screening of 2D materials and rational design of heterojunctions for water splitting photocatalysts, *Small Methods* 2 (5) (2018) 1700359.
- [18] Y. Jing, T. Heine, Two-dimensional Pd 3 P 2 S 8 semiconductors as photocatalysts for the solar-driven oxygen evolution reaction: a theoretical investigation, *J. Mater. Chem. A* 6 (46) (2018) 23495–23501.
- [19] U. Gupta, C. Rao, Hydrogen generation by water splitting using MoS<sub>2</sub> and other transition metal dichalcogenides, *Nano Energy* 41 (2017) 49–65.
- [20] M. Qiao, Y. Chen, Y. Wang, Y. Li, The germanium telluride monolayer: a two dimensional semiconductor with high carrier mobility for photocatalytic water splitting, *J. Mater. Chem. A* 6 (9) (2018) 4119–4125.
- [21] M.S. Burke, L.J. Enman, A.S. Batchellor, S. Zou, S.W. Boettcher, Oxygen evolution reaction electrocatalysis on transition metal oxides and (oxy) hydroxides: activity trends and design principles, *Chem. Mater.* 27 (22) (2015) 7549–7558.
- [22] H. Li, C. Tsai, A.L. Koh, L. Cai, A.W. Contryman, A.H. Fragapane, J. Zhao, H.S. Han, H.C. Manoharan, F. Abild-Pedersen, et al., Activating and optimizing MoS<sub>2</sub> basal planes for hydrogen evolution through the formation of strained sulphur vacancies, *Nature Mater.* 15 (1) (2016) 48–53.
- [23] K.C. Kwon, C. Kim, Q.V. Le, S. Gim, J.-M. Jeon, J.Y. Ham, J.-L. Lee, H.W. Jang, S.Y. Kim, Synthesis of atomically thin transition metal disulfides for charge transport layers in optoelectronic devices, *ACS Nano* 9 (4) (2015) 4146–4155.
- [24] D. Voiry, H. Yamaguchi, J. Li, R. Silva, D.C. Alves, T. Fujita, M. Chen, T. Asefa, V.B. Shenoy, G. Eda, et al., Enhanced catalytic activity in strained chemically exfoliated WS<sub>2</sub> nanosheets for hydrogen evolution, *Nature Mater.* 12 (9) (2013) 850–855.
- [25] D. Singh, N. Khossossi, A. Ainane, R. Ahuja, Modulation of 2D GaS/BTe vdW heterostructure as an efficient HER catalyst under external electric field influence, *Catal. Today* 370 (2021) 14–25.
- [26] L. Jiang, X. Yuan, G. Zeng, J. Liang, Z. Wu, H. Wang, Construction of an all-solid-state Z-scheme photocatalyst based on graphite carbon nitride and its enhancement to catalytic activity, *Environ. Sci.: Nano* 5 (3) (2018) 599–615.
- [27] J. Fu, J. Yu, C. Jiang, B. Cheng, G-C3N4-based heterostructured photocatalysts, *Adv. Energy Mater.* 8 (3) (2018) 1701503.
- [28] F.K. Kessler, Y. Zheng, D. Schwarz, C. Merschjann, W. Schnick, X. Wang, M.J. Bojdys, Functional carbon nitride materials—design strategies for electrochemical devices, *Nat. Rev. Mater.* 2 (6) (2017) 1–17.
- [29] C.B. Ong, L.Y. Ng, A.W. Mohammad, A review of ZnO nanoparticles as solar photocatalysts: Synthesis, mechanisms and applications, *Renew. Sustain. Energy Rev.* 81 (2018) 536–551.
- [30] Y. Li, Y.-L. Li, B. Sa, R. Ahuja, Review of two-dimensional materials for photocatalytic water splitting from a theoretical perspective, *Catal. Sci. Technol.* 7 (3) (2017) 545–559.
- [31] Z. Haman, M. Kibou, I. Bouziani, Y. Benhouria, I. Essaoudi, A. Ainane, R. Ahuja, Structural, electronic and optical properties of two-dimensional janus transition metal oxides MXO (M=Ti, Hf and Zr; X=S and Se) for photovoltaic and opto-electronic applications, *Physica B* 604 (2021) 412621.
- [32] H.L. Zhuang, R.G. Hennig, Computational search for single-layer transition-metal dichalcogenide photocatalysts, *J. Phys. Chem. C* 117 (40) (2013) 20440–20445.
- [33] Y. Cui, L. Peng, L. Sun, Q. Qian, Y. Huang, Two-dimensional few-layer group-III metal monochalcogenides as effective photocatalysts for overall water splitting in the visible range, *J. Mater. Chem. A* 6 (45) (2018) 22768–22777.
- [34] Z. Haman, N. Khossossi, M. Kibou, I. Bouziani, D. Singh, I. Essaoudi, A. Ainane, R. Ahuja, Computational identification of efficient 2D Aluminium chalcogenides monolayers for optoelectronics and photocatalysts applications, *Appl. Surf. Sci.* 556 (2021) 149561.
- [35] C. Tsai, K. Chan, J.K. Nørskov, F. Abild-Pedersen, Rational design of MoS<sub>2</sub> catalysts: tuning the structure and activity via transition metal doping, *Catal. Sci. Technol.* 5 (1) (2015) 246–253.
- [36] S.H. Mir, S. Chakraborty, P.C. Jha, J. Wärnå, H. Soni, P.K. Jha, R. Ahuja, Two-dimensional boron: lightest catalyst for hydrogen and oxygen evolution reaction, *Appl. Phys. Lett.* 109 (5) (2016) 053903.
- [37] A.-Y. Lu, H. Zhu, J. Xiao, C.-P. Chuu, Y. Han, M.-H. Chiu, C.-C. Cheng, C.-W. Yang, K.-H. Wei, Y. Yang, et al., Janus monolayers of transition metal dichalcogenides, *Nature Nanotechnol.* 12 (8) (2017) 744–749.
- [38] Y. Ji, M. Yang, H. Lin, T. Hou, L. Wang, Y. Li, S.-T. Lee, Janus structures of transition metal dichalcogenides as the heterojunction photocatalysts for water splitting, *J. Phys. Chem. C* 122 (5) (2018) 3123–3129.
- [39] Y. Bai, R. Guan, H. Zhang, Q. Zhang, N. Xu, Efficient charge separation and visible-light response of two-dimensional Janus group-III monochalcogenide multilayers, *Catal. Sci. Technol.* 11 (2) (2021) 542–555.
- [40] A. Huang, W. Shi, Z. Wang, Optical properties and photocatalytic applications of two-dimensional Janus group-III monochalcogenides, *J. Phys. Chem. C* 123 (18) (2019) 11388–11396.
- [41] Y. Cui, M. Li, X. Zhang, S. Wang, Y. Huang, Ga<sub>2</sub>O<sub>3</sub> monolayer: A promising hydrogen evolution photocatalyst screened from two-dimensional gallium chalcogenides and the derived janus, *Green Energy Environ.* (2021).
- [42] M. Demirtas, M.J. Varjovi, M.M. Çiçek, E. Durgun, Tuning structural and electronic properties of two-dimensional aluminum monochalcogenides: Prediction of Janus Al 2 X X (X/X : O, S, Se, Te) monolayers, *Phys. Rev. Mater.* 4 (11) (2020) 114003.
- [43] G. Kresse, J. Furthmüller, Efficient iterative schemes for ab initio total-energy calculations using a plane-wave basis set, *Phys. Rev. B* 54 (16) (1996) 11169.
- [44] J. Heyd, G.E. Scuseria, M. Ernzerhof, Hybrid functionals based on a screened Coulomb potential, *J. Chem. Phys.* 118 (18) (2003) 8207–8215.
- [45] A.V. Kruckau, O.A. Vydrov, A.F. Izmaylov, G.E. Scuseria, Influence of the exchange screening parameter on the performance of screened hybrid functionals, *J. Chem. Phys.* 125 (22) (2006) 224106.
- [46] H.J. Monkhorst, J.D. Pack, Special points for Brillouin-zone integrations, *Phys. Rev. B* 13 (12) (1976) 5188.
- [47] S. Grimme, S. Ehrlich, L. Goerigk, Effect of the damping function in dispersion corrected density functional theory, *J. Comput. Chem.* 32 (7) (2011) 1456–1465.
- [48] J. Neugebauer, M. Scheffler, Adsorbate-substrate and adsorbate-adsorbate interactions of Na and K adlayers on Al (111), *Phys. Rev. B* 46 (24) (1992) 16067.
- [49] L. Chaput, A. Togo, I. Tanaka, G. Hug, Phonon-phonon interactions in transition metals, *Phys. Rev. B* 84 (9) (2011) 094302.
- [50] K. Parlinski, Z. Li, Y. Kawazoe, First-principles determination of the soft mode in cubic ZrO<sub>2</sub>, *Phys. Rev. Lett.* 78 (21) (1997) 4063.
- [51] A. Togo, F. Oba, I. Tanaka, First-principles calculations of the ferroelastic transition between rutile-type and CaCl<sub>2</sub>-type SiO<sub>2</sub> at high pressures, *Phys. Rev. B* 78 (13) (2008) 134106.
- [52] M. Parrinello, A. Rahman, Crystal structure and pair potentials: A molecular-dynamics study, *Phys. Rev. Lett.* 45 (14) (1980) 1196.
- [53] L. Kantorovich, N. Rompotis, Generalized Langevin equation for solids. II. Stochastic boundary conditions for nonequilibrium molecular dynamics simulations, *Phys. Rev. B* 78 (9) (2008) 094305.
- [54] D. Singh, P.K. Panda, N. Khossossi, Y.K. Mishra, A. Ainane, R. Ahuja, Impact of edge structures on interfacial interactions and efficient visible-light photocatalytic activity of metal-semiconductor hybrid 2D materials, *Catal. Sci. Technol.* 10 (10) (2020) 3279–3289.
- [55] S. Demirci, N. Avazli, E. Durgun, S. Cahangirov, Structural and electronic properties of monolayer group III monochalcogenides, *Phys. Rev. B* 95 (11) (2017) 115409.

- [56] X. Chen, Y. Huang, J. Liu, H. Yuan, H. Chen, Thermoelectric performance of two-dimensional AlX (X=S, Se, Te): A first-principles-based transport study, *ACS Omega* 4 (18) (2019) 17773–17781.
- [57] M. Gajdoš, K. Hummer, G. Kresse, J. Furthmüller, F. Bechstedt, Linear optical properties in the projector-augmented wave methodology, *Phys. Rev. B* 73 (4) (2006) 045112.
- [58] I. Bouziani, M. Kibbou, Z. Haman, Y. Benhouria, I. Essaoudi, A. Ainane, R. Ahuja, Electronic and optical properties of ZnO nanosheet doped and codoped with Be and/or Mg for ultraviolet optoelectronic technologies: density functional calculations, *Phys. Scr.* 95 (1) (2019) 015804.
- [59] I. Bouziani, Z. Haman, M. Kibbou, I. Essaoudi, A. Ainane, R. Ahuja, Electronic, optical and thermoelectric properties of two-dimensional pentagonal SiGeC<sub>4</sub> nanosheet for photovoltaic applications: First-principles calculations, *Superlattices Microstruct.* 158 (2021) 107024.
- [60] I. Bouziani, M. Kibbou, Z. Haman, N. Khossossi, I. Essaoudi, A. Ainane, R. Ahuja, Two-dimensional Janus Sn<sub>2</sub>S<sub>2</sub> and Sn<sub>2</sub>GeS<sub>2</sub> semiconductors as strong absorber candidates for photovoltaic solar cells: First principles computations, *Physica E* 134 (2021) 114900.
- [61] I. Bouziani, Z. Haman, M. Kibbou, Y. Benhouria, I. Essaoudi, A. Ainane, R. Ahuja, Ab initio study of electronic and optical properties of penta-SiC<sub>2</sub> and SiGeC<sub>4</sub> monolayers for solar energy conversion, *Superlattices Microstruct.* 142 (2020) 106524.
- [62] M.R. Kim, D. Ma, Quantum-dot-based solar cells: recent advances, strategies, and challenges, *J. Phys. Chem. Lett.* 6 (1) (2015) 85–99.
- [63] M. Kibbou, Z. Haman, I. Bouziani, N. Khossossi, Y. Benhouria, I. Essaoudi, A. Ainane, R. Ahuja, Cs<sub>2</sub>InGaX<sub>6</sub> (X=Cl, Br, or I): Emergent Inorganic Halide double Perovskites with enhanced optoelectronic characteristics, *Curr. Appl. Phys.* 21 (2021) 50–57.
- [64] F. Opoku, K.K. Govender, C.G.C.E. van Sittert, P.P. Govender, Understanding the mechanism of enhanced charge separation and visible light photocatalytic activity of modified wurtzite ZnO with nanoclusters of Zns and graphene oxide: from a hybrid density functional study, *J. Chem.* 41 (16) (2017) 8140–8155.
- [65] X. Li, Z. Li, J. Yang, Proposed photosynthesis method for producing hydrogen from dissociated water molecules using incident near-infrared light, *Phys. Rev. Lett.* 112 (1) (2014) 018301.
- [66] L. Ju, J. Shang, X. Tang, L. Kou, Tunable photocatalytic water splitting by the ferroelectric switch in a 2D AgBiP<sub>2</sub>Se<sub>6</sub> monolayer, *J. Am. Chem. Soc.* 142 (3) (2019) 1492–1500.